Behavioral analysis of membrane fouling caused by coexistence of proteins and cations in membrane distillation

Ding, Mingmei, Liu, Beining, Zhang, Sihao, Wang, Ao, Xu, Hang, Gao, Emily, Zhang, Jianhua, Nghiem, Long D and Gao, Li (2026) Behavioral analysis of membrane fouling caused by coexistence of proteins and cations in membrane distillation. Desalination, 621. ISSN 0011-9164

Desalination 621 (2026) 119734

Contents lists available at ScienceDirect

Desalination

journal homepage: www.elsevier.com/locate/desal

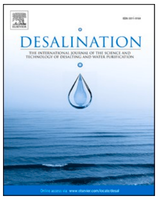

Behavioral analysis of membrane fouling caused by coexistence of proteins and cations in membrane distillation

Mingmei Ding [a], Beining Liu [a], Sihao Zhang [a], Ao Wang [a], Hang Xu [a,*], Emily Gao [b], Jianhua Zhang [c], Long D. Nghiem [d], Li Gao [b,*]

[a] *Ministry of Education Key Laboratory of Integrated Regulation and Resource Development on Shallow Lakes, Hohai University, Nanjing, 210098, China*
[b] *School of Science, RMIT University, Melbourne, Victoria, 3000, Australia*
[c] *Institute for Sustainable Industries and Liveable Cities, Victoria University, Melbourne, VIC, 8001, Australia*
[d] *Centre for Technology in Water and Wastewater, School of Civil and Environmental Engineering, University of Technology Sydney, Ultimo, New South Wales, 2007, Australia*

HIGHLIGHTS

- Coexisting cations aggravate BSA fouling; Na^+ causes stronger fouling than Ca^{2+} or Na^+–Ca^{2+} mixtures.
- The degree of membrane fouling followed the order of BSA < BSA-Ca^{2+} < BSA-Na^+-Ca^{2+} < BSA-Na^+.
- The addition of cations significantly reduces the energy barrier between BSA and the membrane.
- The complexes formed between BSA and Ca^{2+} are more difficult to remove with NaOH.

GRAPHICAL ABSTRACT

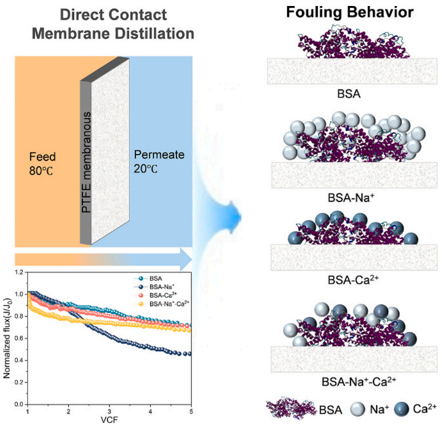

ARTICLE INFO

Keywords:
Membrane distillation
Bovine serum albumin
Sodium ion
Calcium ion
Fouling mechanisms

ABSTRACT

Membrane fouling is a key issue limiting membrane distillation (MD) technology, especially when organic and inorganic fouling coexist and produce complex interactions. In this study, Bovine Serum Albumin (BSA) was employed as a model organic foulant to represent proteinaceous contaminants. The impact of a protein-inorganic salt system on MD performance was investigated by adding inorganic salts with different valencies, namely calcium chloride ($CaCl_2$) and sodium chloride (NaCl). The results indicate that the addition of cations significantly exacerbates membrane fouling and increases the difficulty of cleaning. Na^+ reduces the interaction energy barrier between the membrane and BSA to the lowest level, while facilitating the adsorption of substantial quantities of hydrophobic compounds on the membrane surface, resulting in a thicker fouling layer. In contrast, the presence of Ca^{2+} promotes the adsorption of small molecules onto the membrane surface, forming a more loosely structured and hydrophilic fouling layer. Compared with Na^+-induced fouling, Ca^{2+}-induced fouling

---

* Corresponding authors.
E-mail addresses: xuhang810826@hhu.edu.com (H. Xu), Li.gao@rmit.edu.au (L. Gao).

https://doi.org/10.1016/j.desal.2025.119734
Received 26 August 2025; Received in revised form 2 December 2025; Accepted 3 December 2025

exhibits lower overall severity but shows greater resistance to cleaning. This increased resistance is attributable to BSA—Ca^{2+} bridging complexes, which are more difficult to dislodge during cleaning. In the mixed inorganic salt ion system, the interaction between the two inorganic salt ions produces an intermediate level of contamination compared to the single cation system.

1. Introduction

As the demand for freshwater resources continues to rise, MD has gained considerable attention as a promising desalination technology [1–3]. This process primarily relies on thermal energy to drive vapor molecules through a hydrophobic porous membrane, facilitating separation [4,5]. One side of the membrane is exposed to a heated, high-salinity feed solution, while the opposite side is in contact with a cold permeate stream. The temperature gradient across the membrane induces a vapor pressure difference that drives vapor transport through the membrane, resulting in the condensation of pure water on the permeate side [6,7]. MD can utilize low-grade thermal energy (<100 °C) for seawater desalination, offering significant advantages in cost reduction and energy efficiency [8]. The MD process has four primary configurations: Air Gap MD (AGMD), Direct Contact Membrane Distillation (DCMD), Gas Sweeping MD (GSMD), and Vacuum MD (VMD), all of which share the common characteristic that the feed solution is in direct contact with one side of the membrane [9,10]. DCMD has attracted considerable research interest due to its operational simplicity and the advantage of not requiring an external condenser [11–13].

However, membrane fouling remains a persistent challenge in the advancement of membrane technologies and continues to hinder the development of MD [14]. Unlike pressure-driven membrane filtration processes, MD relies on evaporation, which promotes localized supersaturation and subsequent heterogeneous nucleation of inorganic salts on the membrane surface, thereby inducing scaling [15]. For organic substances, due to the hydrophobic nature of MD membranes, the affinity to hydrophobic organic compounds is stronger [16]. During operation, the membrane surface and pores may become partially or fully fouled and obstructed, resulting in reduced filtration efficiency. Furthermore, the fouling layer introduces additional thermal resistance, thereby reducing the evaporation surface temperature. This reduction in temperature lowers the driving force for vapor permeation, ultimately increasing energy consumption and diminishing overall process efficiency [17,18]. Organic contaminants are often the most challenging type of fouling in MD and primarily consist of proteins [19], polysaccharides [20] and humic substances [21]. Proteinaceous substances are recognized as major contributors to membrane fouling in wastewater treatment, seawater desalination, and water reclamation applications [22]. Protein fouling in MD presents a significant challenge due to the strong affinity between hydrophobic membrane surfaces and protein layers. This interaction can lead to reduced process efficiency and increased operational costs [23].

This is particularly relevant in the dairy industry [24]. Whey effluents and cleaning wastewaters often contain high concentrations of proteins and inorganic ions. BSA exhibits similar interfacial behavior to many natural proteins and is therefore widely used as a model foulant in membrane fouling studies. For instance, Zhai et al. reported that the presence of Na^{+} alone may enhance fouling by weakening electrostatic interactions [25]. Ding et al. pointed out that Ca^{2+} primarily affects the fouling process by increasing the particle size of BSA through a bridging effect [26]. Cai et al. suggested that in high-salinity environments, the addition of Ca^{2+} in the presence of Na^{+} can intensify BSA-induced fouling [27]. Existing studies have predominantly focused on the performance characteristics and mechanisms of BSA, Na^{+}, and Ca^{2+} fouling systems in pressure-driven membrane separation technologies. Numerous studies have investigated the transmembrane flux decline associated with these fouling systems in pressure-driven processes [28,29]. However, due to the distinct separation mechanism of MD, the treatment of wastewater containing both proteins and salt ions yields different fouling phenomena and outcomes compared to pressure-driven membrane filtration systems. There is currently a gap in research on this topic. Therefore, it is essential to elucidate the fouling mechanisms of BSA and cations on the membrane surface through multi-scale analysis to optimize the antifouling performance of MD processes in protein-containing systems.

This study focuses on elucidating the synergistic fouling mechanisms of BSA and inorganic cations during the MD process, aiming to fill the research gap in MD technology. A series of DCMD and membrane cleaning experiments were conducted to investigate the fouling behavior when monovalent Na^{+} and divalent Ca^{2+} coexist with BSA, assessing their impact on membrane fouling. By measuring flux variations and employing multiple characterization techniques, the composition of foulants and the underlying fouling mechanisms were revealed. Pearson correlation heat maps were employed to evaluate the relationships among the key variables. Furthermore, Liquid Chromatography–Organic Carbon Detection (LC-OCD) and extended Derjaguin–Landau–Verwey–Overbeek (XDLVO) theory were employed to further elucidate the fouling mechanisms at the molecular level. These findings have advanced our understanding of protein fouling mechanisms in membrane distillation systems and offer valuable guidance for the cleaning of hydrophobic membranes affected by protein fouling.

2. Materials and methods

2.1. Membrane distillation experimental setup

As illustrated in Fig. S1, the DCMD system primarily comprises two water circulation systems for the cold and hot sides. The custom-fabricated membrane module comprises two identical membrane cells made from polymethyl methacrylate, with an effective membrane area of 45 cm^2. Water circulation on both sides is achieved using a peristaltic pump (DIPump550, Kacuaner Fluid Technology Co., Ltd.) operating at a flow rate of 480 mL/min, resulting in a crossflow velocity of 6.16 cm/s across the membrane. The feed side temperature is maintained at 80 °C using a water bath heater (HHW420, Changzhou Jintan Liangyou Instrument Co., Ltd.). To ensure an appropriate membrane distillation operational flux, the temperature of the MD cold-side low-temperature thermostatic bath (XODC-0506, Nanjing Xianou Instrument Manufacturing Co., Ltd.) is set to 20 °C. Both the feed tank and permeate tank have a volume of 3000 mL, with the feed solution volume set at 2500 mL. Prior to operation, 300 mL of ultrapure water is added to the permeate tank to initiate the cold water circulation. The permeate tank is connected to an online digital balance (DJ2002FT, Kunshan Jinke Hua Electronics Co., Ltd.), with recordings taken every 10 min. To ensure the reliability of the experimental data, each DCMD experiment was conducted in triplicate. The mass increment corresponds to the volume of permeate. The variation in permeate flux is calculated using Eq. (1).

$$J = \frac{V}{A \times T} \tag{1}$$

where J is the permeate flux during membrane distillation operation, measured in $L \cdot m^{-2} \cdot h^{-1}$ (LMH); V is the volume of permeate, measured in liters (L); A is the effective membrane area, measured in square meters (m^2); and t is the operation time, measured in hours (h).

To eliminate errors inherent to the membrane, the specific flux (SF) is calculated using Eq. (2) to characterize the variation in permeate flux.

$$SF = \frac{J}{J_0} \tag{2}$$

Here, J_0 represents the initial permeate flux measured during the first 10 min of operation, with units of $L \cdot m^{-2} \cdot h^{-1}$. The average permeate flux measured within the first ten minutes of operation after the system has reached stable temperature conditions. In each experiment, J_0 is measured using the feed composition employed for that particular run.

As shown in Eq. (3), the volume concentration factor (VCF) is defined as the ratio of the initial feed volume to the total volume of permeate collected through the membrane

$$VCF = \frac{V_0}{V_0 - V_i} \tag{3}$$

where V_0 is the initial feed volume, and V_i is the permeated volume at time i.

2.2. Membranes and experimental reagents

The polytetrafluoroethylene (PTFE) membranes were procured from Haining Wanda Filtration Equipment Co., Ltd., China. These membranes have an average pore size of 0.22 μm, an average thickness of 100 μm, and a porosity of 70 %. BSA, NaCl, $CaCl_2$, sodium hydroxide (NaOH), and hydrochloric acid (HCl) were procured from China Medicine Chemical Reagents Co, Ltd. To accelerate the rate of structure formation, this experiment utilized a BSA solution with a concentration of 150 mg/L [30]. The specific preparation procedure is as follows: deionized water was prepared using an ultrapure water system (UPT-II-10 T, Ulupure, Chengdu, China). After adding the foulants, the mixture was stirred at room temperature for 24 h to prepare the stock solution, and the pH was subsequently adjusted to 7 ± 0.1 using NaOH and HCl [31].

The feed compositions listed in Table 1 are designed as a model protein-salt system representative of protein-rich saline effluents, with BSA (150 mg/L) and Na^+/Ca^{2+} concentrations chosen within the typical ranges used in fundamental fouling studies to ensure measurable flux decline while maintaining a fixed ionic strength (20 mM) across all cation systems. These conditions enable us to focus on the mechanistic effects of Na^+ and Ca^{2+} on the MD process.

2.3. Membrane fouling evaluation

Multiple cyclic filtration operations were commonly employed to evaluate membrane cleaning efficiency. NaOH has been demonstrated to effectively remove organic contaminants from membrane surfaces and restore the membranes to their initial performance [32]. Therefore, all MD experiments in this study employed a cyclic cleaning process, using 1000 mL of permeate per cycle. Subsequently, the fouled membranes were cyclically cleaned with 400 mL of 0.1 mol NaOH solution at a flow rate of 0.2 m/s for 30 min. The cleaned membranes were then subjected to a second cyclic filtration test. Each test concluded after completing cyclic filtration and membrane cleaning, was repeated at least twice, and utilized a new membrane for each trial.

Table 1
Chemical compositions of the feed solution.

Samples	Feed solution	Solution ionic strength (mM)
BSA system	BSA (150 mg/L)	0
BSA-Na^+ system	BSA (150 mg/L), NaCl (20 mM)	20
BSA-Ca^{2+} system	BSA (150 mg/L), $CaCl_2$ (20 mM)	20
BSA-Na^+-Ca^{2+} system	BSA (150 mg/L), NaCl (10 mM), $CaCl_2$ (10 mM)	20

2.4. Analytical methods

Zeta potential and particle size of the feed solution were measured using a Zetasizer instrument (Zetasizer Nano Series Nano-ZS90, Malvern Panalytical, UK and the Netherlands). It should be noted that the zeta potential was measured at 25 ± 1 °C using a Zetasizer Nano-ZS90 instrument, which is incapable of operation at 80 °C. Consequently, the reported values serve solely as comparative indicators of electrostatic interactions between systems, rather than precise in situ measurements at the DCMD operating temperature. Scanning Electron Microscopy (SEM, S-4800, Hitachi, Japan) analyzed fouling morphology on the membrane surface and cross-section. Fourier Transform Infrared Spectroscopy (FTIR, Nicolet iS50, Thermo Fisher Scientific, USA) was employed to detect the vibrational energy of chemical bonds in functional groups within the samples, and membrane foulants were identified based on the characteristic absorption peaks of different functional groups. Energy Dispersive X-ray Spectroscopy (EDS, TESCAN MIRA4, Czech Republic) was used to analyze the elemental composition of the membrane fouling layer. A solid surface zeta potential analyzer (Anton Paar Sur PASS 3, GmbH, Austria) was used to analyze the surface charge of the membranes. A static contact angle goniometer (CAM200, KSV, Finland) was employed to measure the water contact angle on the membrane surface, thereby determining its hydrophilicity or hydrophobicity. The organic composition of the fouling layer was analyzed using LC-OCD. The contaminated membrane was allowed to dry, then cut into pieces and placed into a beaker containing 30 mL of ultrapure water. The beaker was sonicated in an ultrasonic bath at 30 °C for 15 min, and the samples were subsequently filtered through a 0.45 μm injection filter prior to analysis [33].

2.5. XDLVO analysis

The extended XDLVO theory utilizes zeta potential and contact angle measurements to evaluate the surface interaction energies between membranes and foulants, and can be employed to analyze nanometer-scale fouling behaviors [34]. Currently, the XDLVO theory has been applied in the membrane distillation field to investigate fouling processes [35]. The XDLVO theory can be employed to directly quantify the interaction energies between foulants and membrane surfaces, as well as among foulants themselves, in DCMD systems. By quantifying surface tension components and zeta potential, the XDLVO theory can be used to estimate the interaction energy barrier between colloidal interfaces [36]. Its primary advantage lies in its ability to translate interfacial physicochemical parameters into directly quantifiable interaction energy profiles for comparative analysis. However, the XDLVO theory only applies to smooth planes and cannot accurately quantify the short-range interfacial energy [37].

3. Results and discussion

3.1. Zeta potential and particle size distribution

As shown in Fig. 1a, the zeta potential values for the BSA, BSA—Na^+, BSA—Ca^{2+}, and BSA-Na^+-Ca^{2+} feed solutions are all negative. The measured zeta potential of the PTFE membrane surface is −61.7 mV. In the BSA solution, the zeta potential was −32.17 mV, indicating significant electrostatic repulsion between the negatively charged BSA and the PTFE membrane during the MD process. With the addition of inorganic salts, more charges were introduced into the system. The negative functional groups were shielded due to double-layer compression and a reduction in fixed layer charges. In the BSA—Na^+ system, the zeta potential decreased to −14.5 mV, indicating a reduction in negative charges. However, electrostatic repulsion between organic molecules still predominated, maintaining a well-dispersed state. Upon the addition of Ca^{2+}, the zeta potential of the solution decreased to −7.56 mV, which is attributed to interactions between Ca^{2+} and adjacent carboxyl

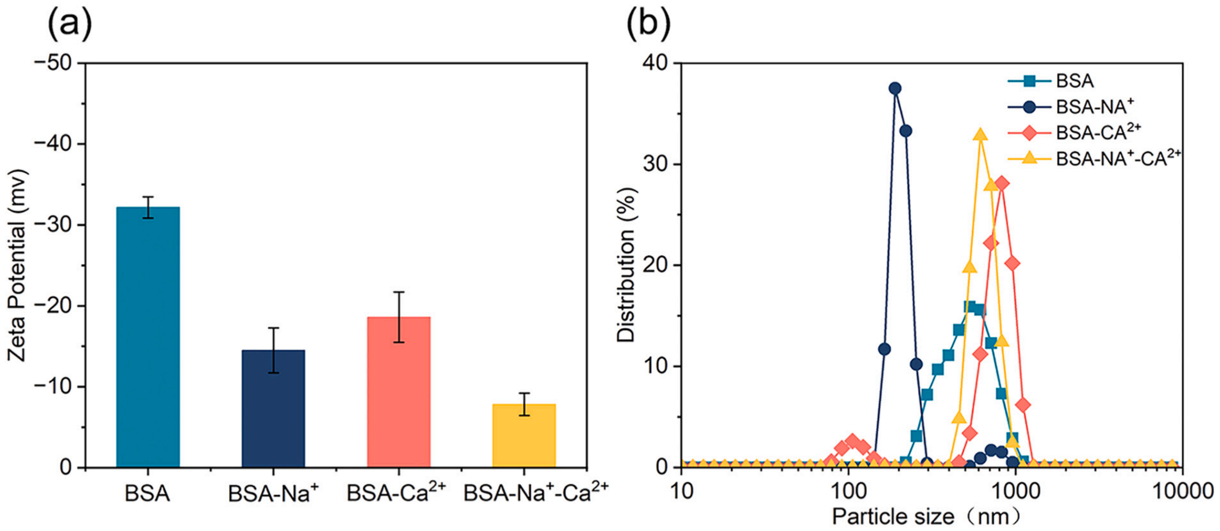

Fig. 1. (a) Zeta potential and (b) particle size distribution of four solutions: BSA, BSA—Na^+, BSA—Ca^{2+}, and BSA-Na^+-Ca^{2+}.

groups on different BSA peptide chains, thereby reducing the overall negative charge of the system [23]. The zeta potential in the BSA-Na^+-Ca^{2+} system further decreases to −6.26 mV, attributed to the synergistic effect of Ca^{2+} and Na^+.

Zeta potentials were simultaneously measured across a range of pH values (Table.S2). A pH of 7.0 was chosen to ensure BSA stability and to simulate typical near-neutral aqueous environments. At this pH, electrostatic interactions cause repulsion between BSA molecules and the PTFE membrane. In the presence of Na^+, the zeta potential decreases to −14.5 mV as a result of electric double-layer compression, which promotes compact adsorption. The presence of Ca^{2+} further reduces the zeta potential to −7.56 mV through charge shielding and coordination bridging among carboxyl groups, resulting in the formation of larger aggregates. Consequently, under neutral pH conditions, the dominant fouling mechanism transitions from electrostatic repulsion (BSA) to double-layer compression (BSA—Na^+) and ionic bridging (BSA—Ca^{2+}).

In the BSA system, the solution maintained a high level of transparency, indicating the good stability of BSA. However, after the experiment began, a large amount of white flocculent precipitate was observed in the BSA—Ca^{2+} and BSA-Na^+-Ca^{2+} systems. This occurs because BSA undergoes conformational changes at high temperatures, exposing certain groups that may form complexes with Ca^{2+} [29]. The effect of cations on the BSA solution can be analyzed through the particle size distribution, as shown in Fig. 1b. The average size of BSA alone as the feed solution was approximately 514 nm. Due to the negatively charged single organic substance in the solution, electrostatic repulsion between colloids reduced the level of aggregation. Upon the addition of Na^+, the particle size decreases to 348 nm due to the compression of the electrical double layer. In contrast, due to the “bridging effect” of Ca^{2+}, the average particle size in the BSA—Ca^{2+} system increases to 690 nm. The ‘bridging effect’ refers to divalent cations coordinating with negatively charged functional groups on BSA molecules, causing dispersed colloids to bridge together into larger, stable aggregates [38]. This occurs as Ca^{2+} facilitates the cross-linking of organic molecules, promoting particle aggregation and growth [39]. In the mixed system, the particle size increased to 773 nm. This is primarily attributed to the synergistic effect of Na^+ and Ca^{2+}. It can be observed that the addition of cations reduces the overall zeta potential of the solution, thereby weakening electrostatic interactions. Na^+ reduces the size of compound molecules through the double-layer compression effect, leading to a decrease in particle size in the BSA—Na^+ system. In contrast, Ca^{2+}, due to its bridging effect surpassing electrostatic interactions, results in an increased particle size in the BSA—Ca^{2+} system. In the mixed system, Na^+ may weaken the bridging effect, thereby reducing the degree of molecular aggregation.

3.2. DCMD experiment

Fig. 2a shows the variations in membrane flux for the four systems. For the single BSA solution, the flux decrease was minimal, resulting in a final membrane specific flux of 0.72. When cations were added, the membrane flux decreased significantly. The initial decrease was notable, but the trend stabilized as the device operated. The data indicate a descending order of membrane flux decrease as follows: BSA system < BSA- Ca^{2+} system < BSA-Na^+-Ca^{2+} system < BSA—Na^+ system. Na^+ causes severe membrane fouling of BSA, affecting the MD process and reducing the final membrane specific flux to 0.46. Due to the bridging effect with BSA, Ca^{2+} caused protein aggregation and deposition in the feed solution, alleviating membrane fouling compared to Na^+. The addition of cations reduces the zeta potential of BSA molecules, resulting in decreased electrostatic repulsion between the membrane and foulants, thereby promoting fouling formation. Additional DCMD experiments were performed for all four systems at feed temperatures of 70 and 60 °C (Fig. S4). At the lower feed temperatures, the overall flux decline was mitigated owing to the reduced driving force and slower fouling kinetics; however, the relative fouling sequence remained unchanged.

It is noteworthy that, although the addition of Na^+ and Ca^{2+} reduces the magnitude of the negative zeta potential of BSA, the fouling behavior in DCMD does not simply follow this electrostatic trend: the BSA—Na^+ system exhibits the most severe flux decline, whereas the BSA—Ca^{2+} system shows markedly milder attenuation. This apparent discrepancy indicates that zeta potential alone is insufficient to predict fouling severity. Electrostatic interactions therefore provide only a first-order description of BSA-cation interactions and do not constitute the dominant fouling mechanism in this system.

As shown in Fig. 2b, the permeate conductivity of all systems remained below 3 μS·cm^{-1}, which is well within the range previously associated with stable DCMD operation and high-quality distillate without significant pore wetting [40]. Minor variations in initial conductivity values (≈1.5–2.3 μS cm^{-1}) and subsequent slopes among the four systems were attributed to localized partial wetting phenomena during the start-up process [41]. Under higher VCF conditions, the BSA—Na^+ and BSA-Na^+-Ca^{2+} systems exhibited a slight increase in conductivity. This may stem from Na^+-induced double-layer compression, promoting denser yet uneven fouling deposition while triggering partial pore wetting. In contrast, Ca^{2+}-induced fouling layers exhibited greater porosity and hydrophilicity, thereby inhibiting the wetting

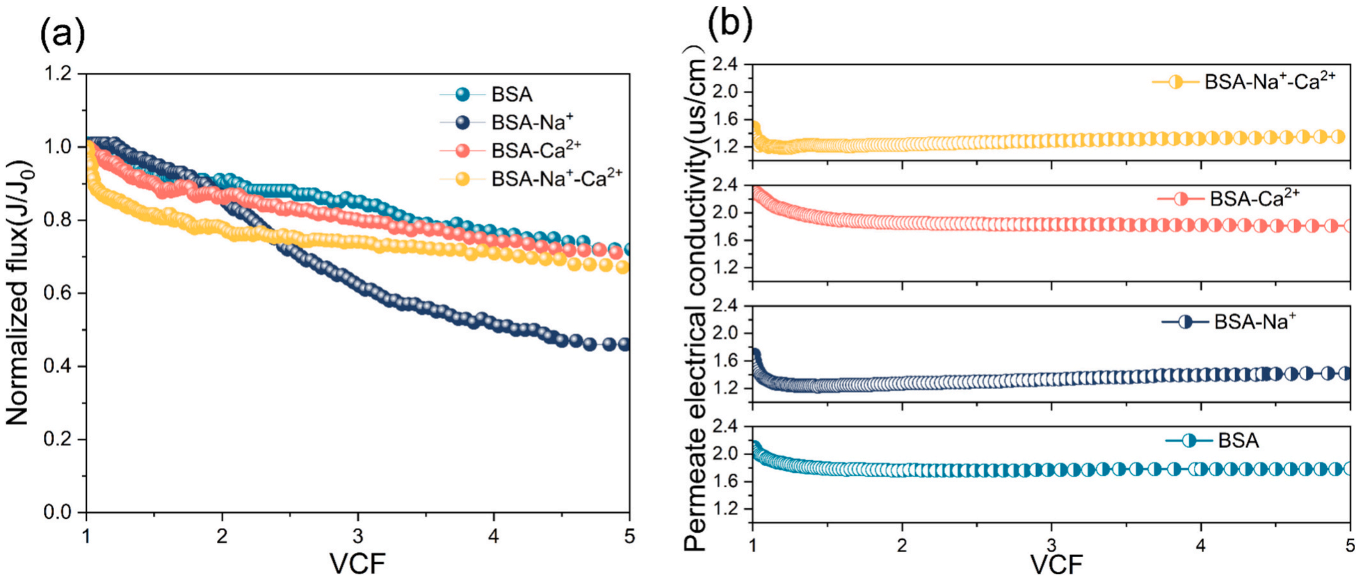

Fig. 2. (a) Variations in the normalized water flux with the concentration factor in the DCMD test. (b) Permeate electrical conductivity with the concentration factor in the DCMD test.

process. Overall, despite partial fouling occurring on the membrane surface during the DCMD process, the integrity of the membrane pores remains largely unaffected by wetting. Consequently, the membrane continues to effectively separate the majority of inorganic salt ions.

3.3. Fouled membrane analysis

3.3.1. Topographic characterization

The original PTFE membrane comprises a loose nonwoven fabric support layer and a thinner PTFE active layer, displaying a characteristic fibrous nodular microporous structure with clearly discernible pores (Fig. S4). As shown in Fig. S6, at VCF = 1.5, only dispersed BSA aggregates were observed on the membrane surface in the pure BSA system, whereas the BSA—Na$^+$ system had already developed a nearly continuous granular layer. In contrast, the BSA—Ca^{2+} system formed a loose, porous, flocculent network, while the mixed BSA-Na$^+$-Ca^{2+} system exhibited an incipient yet relatively smooth deposit layer. As the VCF increased to 5 (Fig. 3), these deposits progressively evolved: the pure BSA system developed a dense layer of approximately 0.6 μm; the BSA—Na$^+$ system formed a compact, cake-like layer of 23 μm; the BSA—Ca^{2+} system produced a porous structure of 1.8 μm; and the mixed system generated an intermediate deposit layer of 3.4 μm. The progressive growth and densification observed at VCF = 1.5 and 5 are consistent with the flux distribution curves in Fig. 2a: the early-formed, thick, dense Na$^+$-induced fouling layer causes the greatest flux decline, whereas the looser Ca^{2+}-induced filter cake, despite its greater dry thickness, imposes a lower hydraulic resistance. The thin BSA layer in the single-solute system corresponds to only a minimal flux loss. Overall, these observations demonstrate that interactions between BSA and inorganic salt ions markedly accelerate membrane fouling.

It should be noted that the fouling layer thicknesses presented herein were determined from SEM images of dried membrane samples collected following DCMD experiments. During the drying process required for SEM preparation, dehydration of proteins and inorganic fouling matrix may occur, leading to fouling layer shrinkage. Consequently, the measured values underestimate the actual in-situ hydration thickness present during membrane operation. Nevertheless, as all membranes underwent identical drying and imaging procedures, the relative thickness variations observed across the BSA, BSA—Na$^+$, BSA—Ca^{2+}, and BSA-Na$^+$-Ca^{2+} systems retain comparative value for assessment.

3.3.2. Chemical composition of fouling layers

The functional group changes on the membrane surface after MD filtration were analyzed using FTIR. Fig. 4 illustrates two characteristic peaks were observed at 1205 cm^{-1} and 1150 cm^{-1}, corresponding to the stretching vibrations of the F-C-F group [42]. The fouled membrane displayed additional characteristic peaks indicative of proteinaceous organic matter. Specifically, a peak at 1650 cm^{-1} corresponds to the C═O (amide I) group, and another peak at 1550 cm^{-1} corresponds to the N—H (amide II) group. The amide I and amide II bands are unique to the secondary structure of proteins [43]. Furthermore, a hydrophilic feature was observed at 3300 cm^{-1}, which can be attributed to the stretching vibrations of O—H and N—H bonds. In the BSA-Na$^+$-Ca^{2+} system, significant changes at 3300 cm^{-1} were primarily due to the stretching vibrations of N—H and O—H bonds in BSA amino acid residues, leading to alterations in peak shape and intensity. This suggests that the presence of mixed inorganic salts may affect the hydrogen bonding network among protein molecules [44]. The characteristic peaks of C—H bonds at 2930 cm^{-1} and 2850 cm^{-1} remained relatively stable, as these vibrations are typically unaffected by ionic strength. However, variations were observed at the C═O stretching vibration of the peptide backbone at 1650 cm^{-1}, likely due to interactions between metal ions and peptide bonds, indicating possible alterations in the resonance structure of the peptide bonds [45]. The amide II band near 1550 cm^{-1}, reflecting the bending vibration of the N—H bond and the stretching vibration of the C—N bond, exhibited changes in peak shape and position, potentially indicating modifications in BSA's secondary structure [46].

EDS mapping analysis (Table S2) revealed that the pristine membrane primarily consists of C, O, and F elements, which are the main constituents of PTFE. On the surface of the fouled membrane, a significant presence of C and O elements was observed, indicating that the membrane was fouled by organic matter. In the BSA—Ca^{2+} system, the relatively high proportion of Ca^{2+} further confirms its strong binding ability through the bridging effect. In the BSA—Na$^+$ system, the relatively low proportion of Na$^+$ indicates its weaker binding affinity, with most Na$^+$ existing in a free state.

3.3.3. Hydrophobicity/hydrophilicity analysis

Fig. 5 illustrates the changes in water contact angle relative to the pristine membrane. Single BSA fouling reduces the water contact angle of the membrane surface to 41.5°, as hydroxyl (-OH) and amino (-N-H)

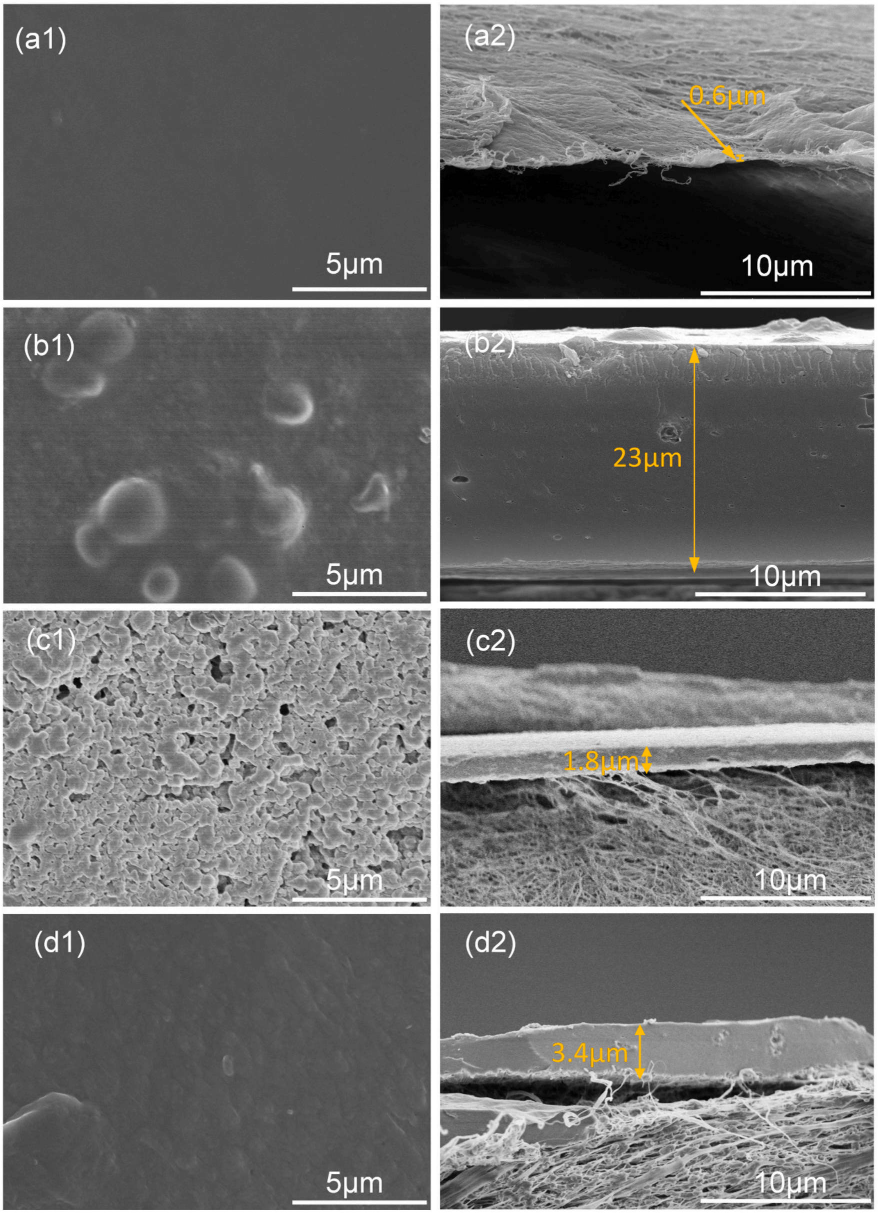

Fig. 3. SEM images of surface and cross-sections of contaminated membranes for (a) BSA, (b) BSA—Na^+, (c) BSA—Ca^{2+}, and (d) BSA-Na^+-Ca^{2+} systems.

groups in the protein enhance membrane hydrophilicity. After the introduction of inorganic salt ions, the decrease in water contact angle becomes more pronounced. In the BSA—Ca^{2+} system, the water contact angle decreases to 35.7° due to Ca^{2+} binding strongly to hydrophilic sites in organic matter, resulting in an overall increase in hydrophilicity [47]. In comparison, the water contact angle in the BSA—Na^+ system decreases to 37.8°, as Na^+ primarily exists in a free state with weaker binding affinity. In the BSA-Na^+-Ca^{2+} system, the water contact angle decreased to 37.8°, which is essentially the same as that observed for the BSA—Na^+ system. This indicates that the mixed-cation fouling layer is comparably hydrophilic, and no additional measurable change in the macroscopic contact angle can be resolved upon introducing Ca^{2+}.

3.4. XDLVO theory

The XDLVO theory is a valuable method for evaluating the thermodynamic interactions of fouling with membrane surfaces and is increasingly used to explore contamination mechanisms in membrane filtration processes. According to the XDLVO theory, thermodynamic interaction is divided into three parts: Lifshitz-van der Waals (LW) interaction, Lewis acid-base (AB) interaction and electrostatic double layer (EL) interaction [36].

3.4.1. Contaminants and membranes

According to the XDLVO theory, a positive interaction energy between the membrane and contaminants indicates repulsive forces, suggesting strong antifouling properties. Conversely, a negative interaction energy signifies attractive forces that can accelerate fouling. Thus, a more negative interaction energy corresponds to a greater impact, resulting in more severe membrane fouling [48]. From Fig. 6, it can be observed that $\Delta G_{\mathrm{flm}}^{\mathrm{LW}}$ is positive, indicating that the LW interaction energy primarily acts as a repulsive force. In contrast, both $\Delta G_{\mathrm{flm}}^{\mathrm{AB}}$ and $\Delta G_{\mathrm{flm}}^{\mathrm{EL}}$ are negative, suggesting attractive interactions that exacerbate membrane fouling. Notably, when colloids near the membrane surface dominate the fouling process, the absolute value of the AB interaction energy is the largest, indicating that AB interaction energy is the primary contributor to the total interaction energy [49]. This is also evidenced by

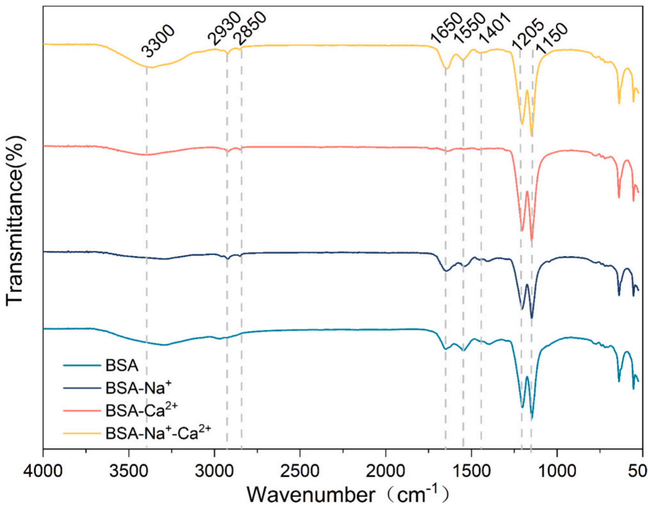

Fig. 4. FTIR spectra of fouled membranes under different conditions.

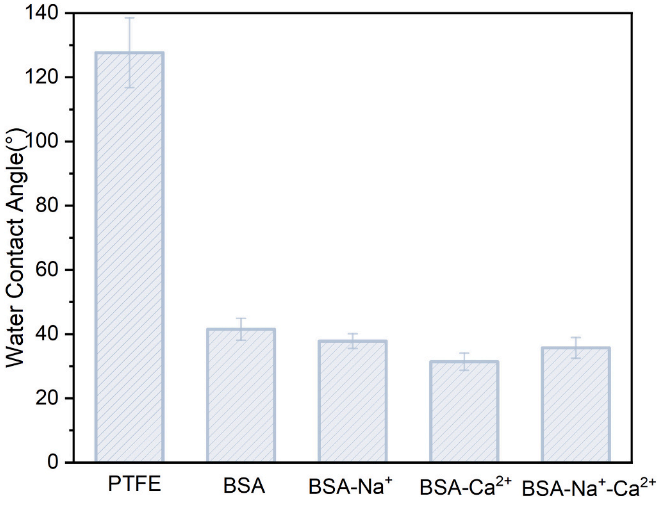

Fig. 5. Water contact angle of PTFE membranes and four feed liquids.

the fact that the trend of $\Delta G_{\text{flm}}^{\text{AB}}$ is similar to that of $\Delta G_{\text{flm}}^{\text{TOT}}$. This suggests that, at the membrane-foulant interface stage, the contact angle exerts a greater influence on membrane fouling compared to zeta potential. The results show that all three interaction energies (AB, EL, and LW) increase as the separation distance decreases. The cumulative value of these energies constitutes the total interfacial free energy. The maximum positive value indicates the minimum energy required to overcome the mutual repulsive force between the contaminant and the membrane, known as the energy barrier. If the contaminant's energy exceeds this value, it is more likely to deposit on the membrane surface. The energy barrier for the single BSA system was found to be relatively high (868.00 kT). However, upon the addition of inorganic salt ions, the energy barrier decreases significantly. Specifically, the energy barrier values for the BSA—Na$^+$, BSA—Ca^{2+}, and BSA-Na$^+$-Ca^{2+} systems are reduced to 222.26 kT, 286.52 kT, and 229.77 kT, respectively. These findings suggest that interactions between BSA and Na$^+$ or Ca^{2+} ions promote pollutant deposition on the membrane surface. Moreover, the energy barrier associated with Na$^+$ is lower than that of Ca^{2+}, indicating that Na$^+$ reduces the system's energy barrier, making it easier to overcome and thereby increasing membrane susceptibility to fouling.

3.4.2. *Contaminants and contaminated membranes*

Fig. 7 illustrates the energy variation of interactions between the fouling and the fouling layer. Since the value of EL differs by orders of magnitude from those of AB and LW, it is not considered. This suggests that, during both the fouling layer and foulant stages, the zeta potential of the foulants has a limited impact on membrane fouling. It is clear that the LW interaction energy is negative, indicating that it is primarily adsorptive and increases as the distance decreases. In contrast, the interaction energies of AB are positive and increase gradually. The total interfacial interaction between contaminants is governed by both the LW and AB energies, which increase as the distance decreases and grow more rapidly at closer separation distances. The results suggest that the repulsive energy barrier between the contaminant and the fouling layer disappears, resulting in a positive total interfacial interaction energy. As a result, contaminant deposition is inhibited in the later stages of membrane fouling, leading to a gradual reduction in the rate of flux decline, consistent with experimental membrane flux data. A stronger repulsive force results in looser bonding between contaminants, primarily forming a reversible fouling layer. When the distance between contaminants and the fouling layer decreases sufficiently, the strong repulsive force persists [50].

The XDLVO theory effectively elucidates the impact of Na$^+$ and Ca^{2+} ions on interfacial interactions. During the early stages of fouling, Na$^+$ demonstrates a greater ability to lower the energy barrier than Ca^{2+}, facilitating the accumulation of foulants on the membrane surface. In the later stages, the total interaction energy transitions from negative to positive, forming a dynamic energy barrier that impedes further foulant deposition.

3.5. *Correlation analysis*

The Pearson correlation coefficient is a dimensionless statistical metric that quantifies the strength of the linear relationship between two continuous variable [51]. The Pearson correlation coefficient r is commonly calculated using the following formula:

$$\boldsymbol{r} = \frac{\sum_{i=1}^{n}(\boldsymbol{x_i}-\overline{\boldsymbol{x}})(\boldsymbol{y_i}-\overline{\boldsymbol{y}})}{\sqrt{\sum_{i=1}^{n}(\boldsymbol{x_i}-\overline{\boldsymbol{x}})^2}\sqrt{\sum_{i=1}^{n}\left(\boldsymbol{y_i}-\overline{\boldsymbol{y}}\right)^2}} = \frac{\boldsymbol{Cov}(\boldsymbol{X},\boldsymbol{Y})}{\boldsymbol{\sigma_X\sigma_Y}} \tag{4}$$

where $\overline{\boldsymbol{x}}$ and $\overline{\boldsymbol{y}}$ are the sample means, $\boldsymbol{\sigma_X}$ and $\boldsymbol{\sigma_Y}$ are the sample standard deviations, and Cov (X, Y) is the sample covariance between variables X and Y. When $r > 0$, the variables are positively correlated; conversely, when $r < 0$, X and Y are negatively correlated.

As shown in Fig. 8, the interaction energy barrier and membrane flux exhibit a positive correlation, with a Pearson correlation coefficient of 0.59. However, this moderate correlation arises because the energy barrier in this context represents the interaction energy between the membrane and foulants, which primarily influences the initial membrane flux. In contrast, the interaction energy barrier shows a strong negative correlation with the solution zeta potential ($r = -0.75$) and an even stronger negative correlation with the membrane surface zeta potential ($r = -0.94$), underscoring the critical role of electrostatic repulsion during the early stages of fouling.Furthermore, Na$^+$ concentration exhibits a strong negative correlation with membrane flux ($r = -0.86$), suggesting that Na$^+$ significantly contributes to membrane fouling. In comparison, Ca^{2+} concentration displays a strong positive correlation with particle size ($r = 0.96$) and a moderate positive correlation with zeta potential ($r = 0.6$), indicating that Ca^{2+} facilitates particle aggregation and enhances charge density through bridging interactions.

3.6. *LC-OCD analysis*

LC-OCD is a powerful technique for characterizing complex natural organic matter (NOM); in this study, it is applied to a model protein (BSA), to gain specific insight into its transformation and interactions

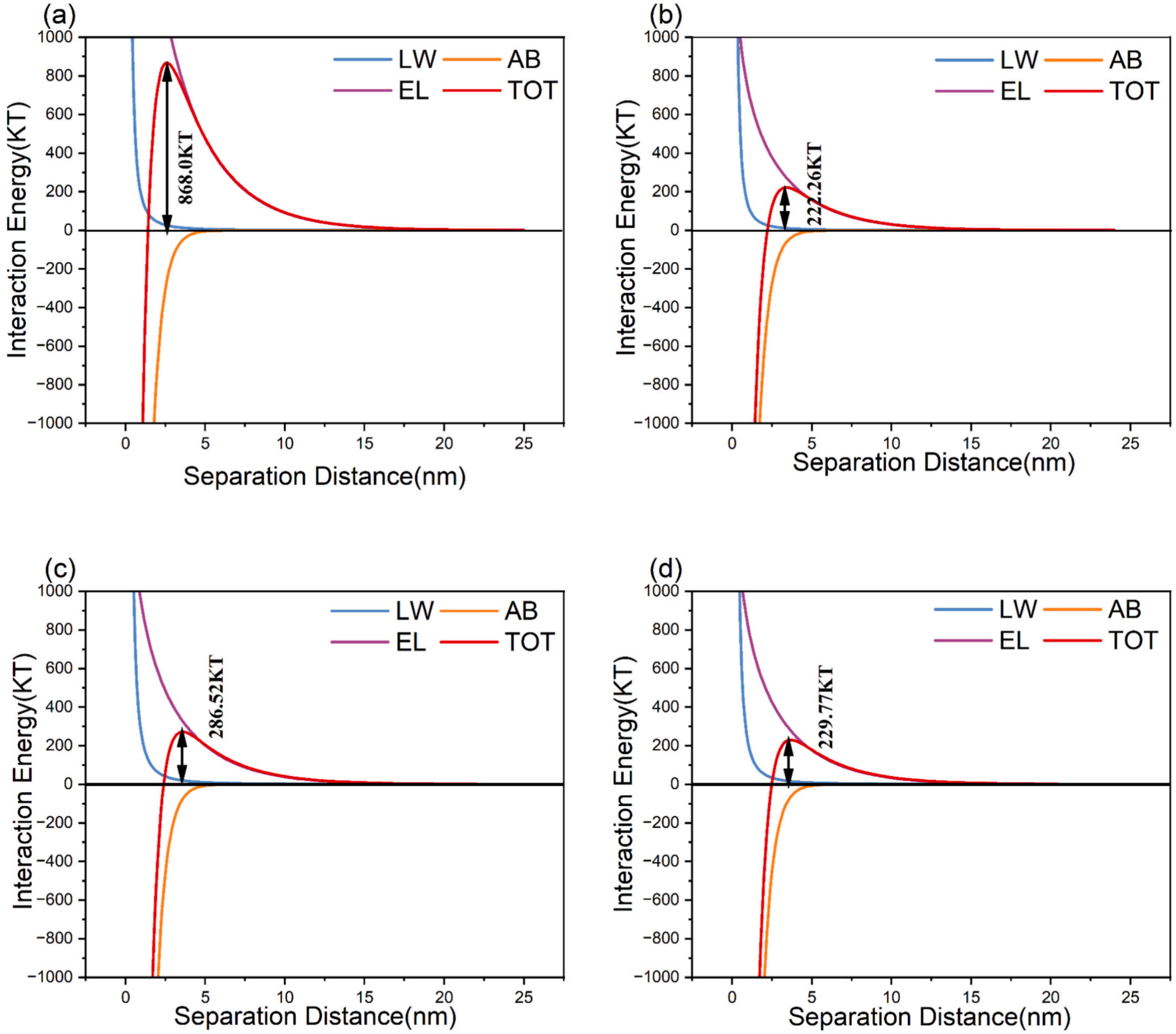

Fig. 6. Foulant-membrane interaction energies for (a) BSA, (b) BSA—Na^+, (c) BSA—Ca^{2+}, and (d) BSA-Na^+-Ca^{2+} systems.

with cations [52]. Generally, NOM could be categorized into five groups according to the molecular weight associated with specific biopolymer fractions: biopolymers (primarily hydrophilic polysaccharides and proteinaceous nitrogen-containing subfractions), humic substances (mainly aromatic macromolecules), building blocks (oxidized or photodegraded fragments of humic substances), low-molecular weight acids (LMW Acids, low molecular weight aliphatic organic acids), and low molecular weight neutrals (LMW Neutrals, including neutral alcohols, aldehydes, ketones, and small amino acids) [53,54].

Within the LC-OCD framework, chromatographically determined dissolved organic carbon (CDOC) denotes the dissolved organic carbon fraction retained and separated by size-exclusion chromatography columns. Hydrophobic organic carbon (HOC), by contrast, is defined as the residual DOC fraction that cannot be chromatographically separated and therefore fails to elute from the column, representing strongly hydrophobic organic matter. By quantitatively tracking the evolution of CDOC sub-fractions in the feed solutions and fouling layers, together with the formation and accumulation of HOC, LC-OCD provides molecular-level insight into membrane fouling mechanisms.

3.6.1. HOC evolution and redistribution

The concentration of dissolved organic carbon (DOC) decreases after the addition of cations, which may be attributed to a shift in BSA from a detectable molecular state to an aggregated or deposited form that cannot be detected by LC-OCD (Table S3). As shown in Fig. 9, chromatographic analysis detected only dissolved organic carbon (DOC) in all four feed solutions. Although DOC remained the dominant fraction in the fouling layer, the emergence of HOC was a key contributor to membrane fouling. This phenomenon may result from the partial thermal decomposition of BSA molecules in the feed solution. In the BSA—Na^+ system, HOC constituted 38 % of the DOC, reaching 1018 μg C L^{-1}—the highest among all systems, indicating that Na^+ enhances the adsorption of hydrophobic foulants onto the membrane surface. In contrast, the BSA—Ca^{2+} system shows a lower HOC proportion of 21 %, with a concentration of 664 μg C/L. Although the BSA-Na^+-Ca^{2+} system exhibits a higher HOC proportion (44 %), the total DOC concentration significantly decreases to 1653 μg C/L(Table S3), likely due to competitive interactions between Ca^{2+} and Na^+ that reduce the membrane's adsorption capacity for organic foulants.

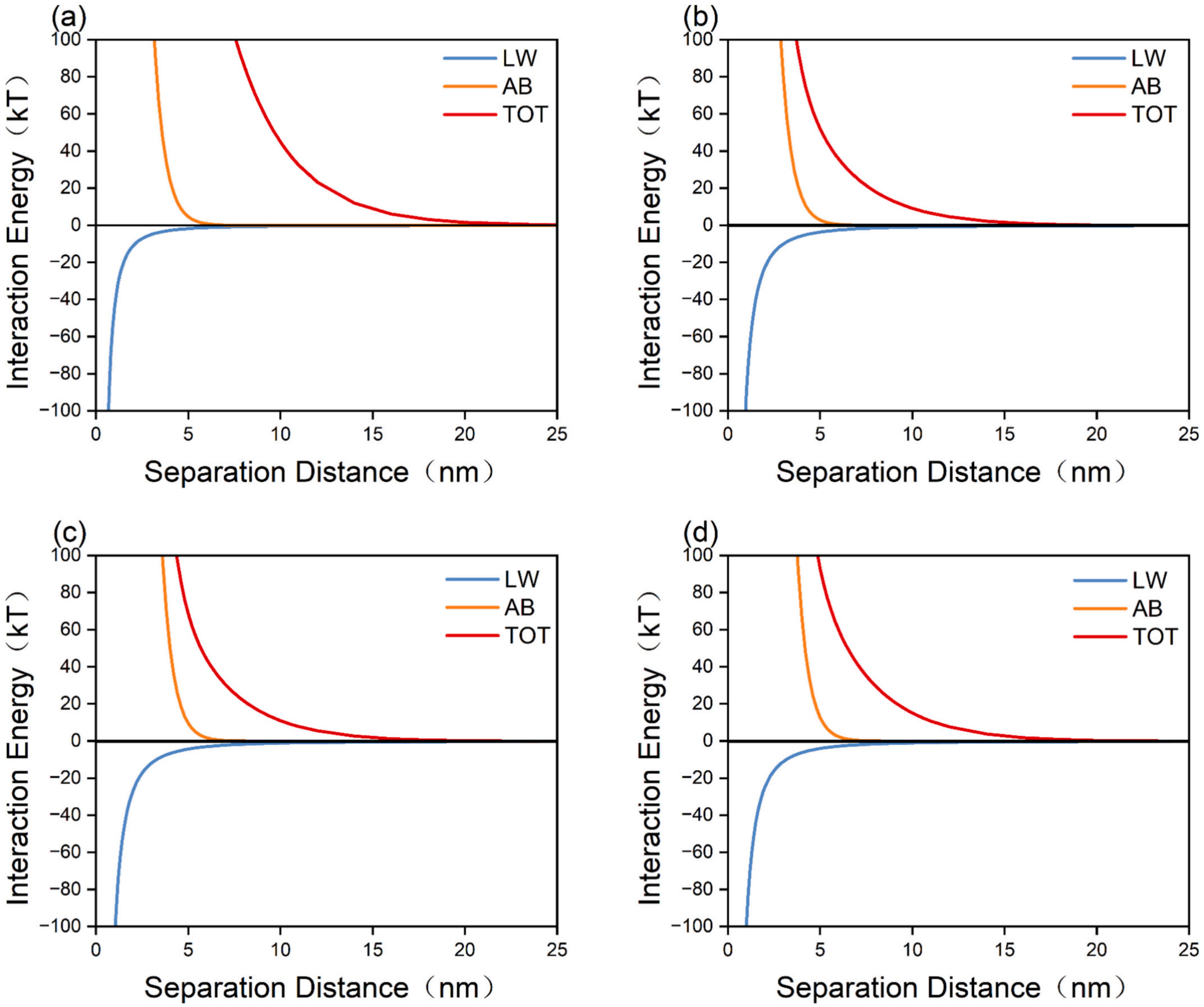

Fig. 7. Pollutants-contaminated layers interaction energies for (a) BSA, (b) BSA—Na^+, (c) BSA—Ca^{2+}, and (d) BSA-Na^+-Ca^{2+} systems.

3.6.2. CDOC fraction shifts and implications for fouling interactions

The changes in CDOC composition before and after fouling are illustrated in Fig. 10. The abundance of biopolymers decreased markedly across all four systems, whereas the fraction of LMW Neutrals compounds increased. This observation indicates that electrostatic repulsion between the fouling layer and incoming foulants is markedly reduced, consistent with the XDLVO results, which demonstrates that EL interactions contribute negligibly to the overall energy barrier during fouling-layer-foulant interactions. Relative to the feed solution, the biopolymer fraction in the BSA—Na^+ system declined from 72 % to 29 %, the building-block fraction fell from 17 % to 2 %, and the proportion of LMW Neutrals species rose from 10 % to 68 %, suggesting that elevated temperature facilitated the depolymerization of compounds with molecular mass > 350 Da into smaller molecules In the BSA—Ca^{2+} system, every component except LMW Neutrals species was nearly eliminated relative to the feed solution, while the proportion of LMW Neutrals increased sharply from 1 % to 93 %. This result suggests that Ca^{2+} promotes the preferential adsorption of neutral small molecules onto the membrane surface. In the BSA-Na^+-Ca^{2+} system, the biopolymer fraction declined from 73 % to 4 %, whereas the building-block fraction remained essentially unchanged. Concurrently, the proportions of LMW Neutrals and LMW Acids species increased from 14 % to 59 % and from 1 % to 24 %, respectively. This distribution is likely driven by competitive adsorption between Na^+ and Ca^{2+}, which induces partial precipitation of macromolecules while moderately enriching LMW compounds.

Overall, BSA—Na^+ system exhibited the highest concentration of HOC, indicating that Na^+ promotes the accumulation of hydrophobic species on the membrane surface and thereby aggravates fouling. By comparison, the BSA—Ca^{2+} system showed the highest level of CDOC, dominated by LMW Neutrals compounds. These findings imply that Ca^{2+} facilitates the breakdown of macromolecules and enhances the adsorption of small neutral molecules onto the membrane, producing a fouling layer composed predominantly of LMW Neutrals species. In the mixed BSA–Na^+–Ca^{2+} system, competitive interactions between the two cations temper their individual effects, yielding an intermediate degree of fouling.

3.7. Membrane cleaning efficiency

To investigate the effect of Na^+ and Ca^{2+} on membrane cleaning efficiency, cleaning tests were conducted on contaminated hydrophobic PTFE membranes using NaOH. Membrane flux decreased during both cycles. During the first filtration cycle, membrane flux decreased rapidly

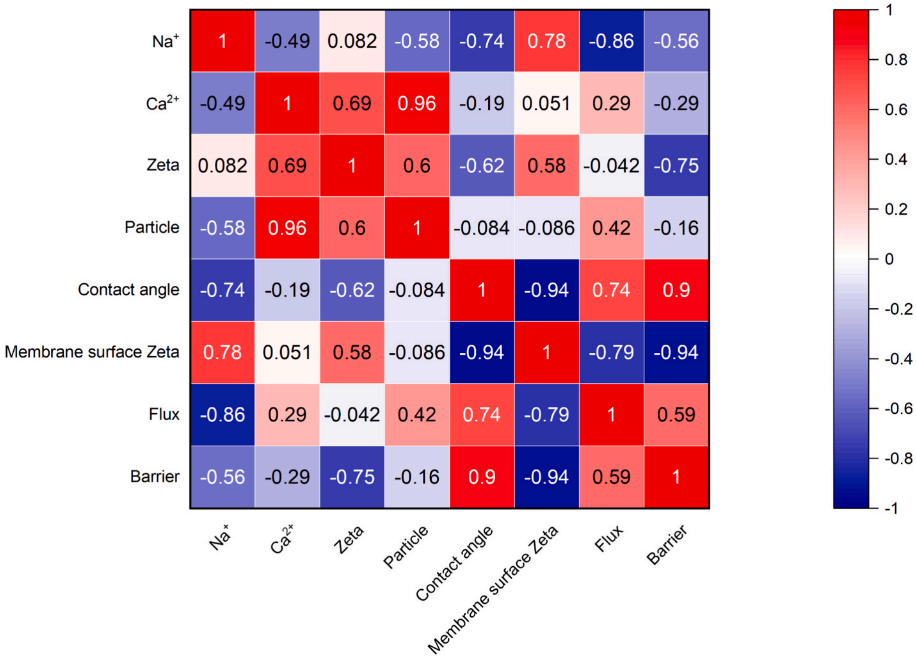

	Na+	Ca2+	Zeta	Particle	Contact angle	Membrane surface Zeta	Flux	Barrier
Na+	1	-0.49	0.082	-0.58	-0.74	0.78	-0.86	-0.56
Ca2+	-0.49	1	0.69	0.96	-0.19	0.051	0.29	-0.29
Zeta	0.082	0.69	1	0.6	-0.62	0.58	-0.042	-0.75
Particle	-0.58	0.96	0.6	1	-0.084	-0.086	0.42	-0.16
Contact angle	-0.74	-0.19	-0.62	-0.084	1	-0.94	0.74	0.9
Membrane surface Zeta	0.78	0.051	0.58	-0.086	-0.94	1	-0.79	-0.94
Flux	-0.86	0.29	-0.042	0.42	0.74	-0.79	1	0.59
Barrier	-0.56	-0.29	-0.75	-0.16	0.9	-0.94	0.59	1

Fig. 8. Pearson correlation heat map.

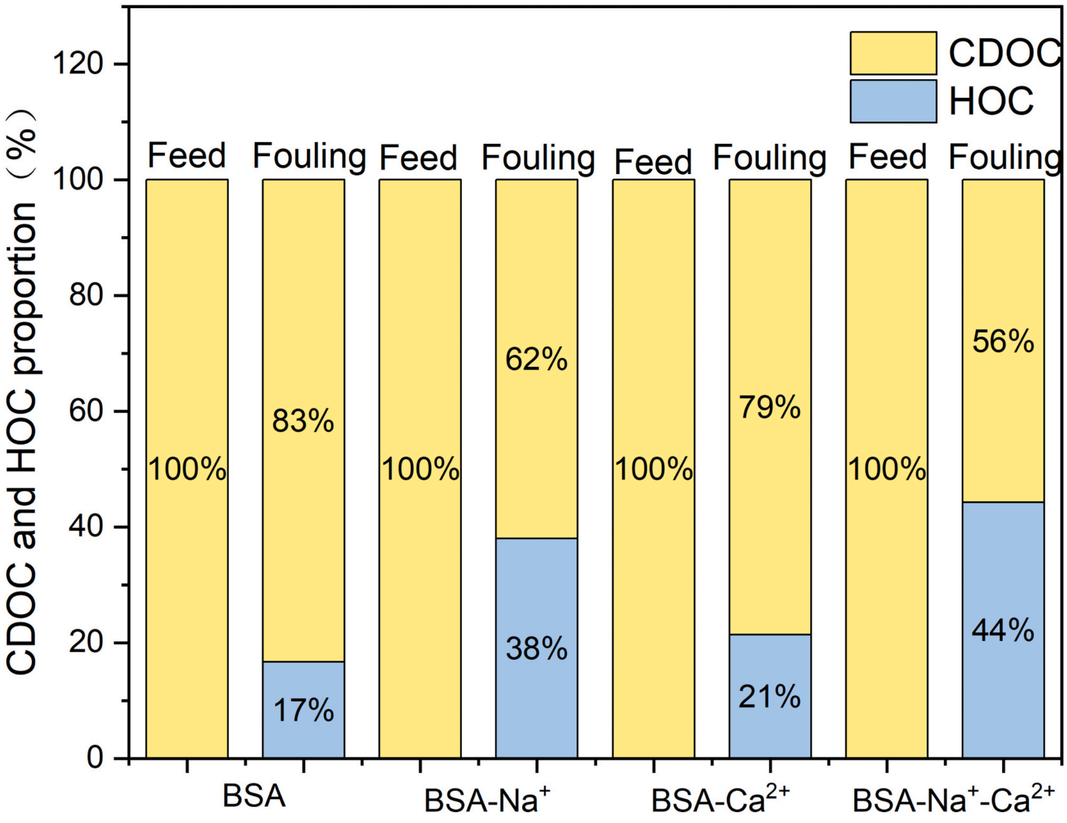

Fig. 9. Proportion of HOC and CDOC components in feed liquid and fouling liquid.

due to the deposition of foulants. At this stage, the water contact angles on the membrane surface were 79.7°, 54.8°, 64.6°, and 66.9° for the BSA, BSA—Na$^+$, BSA—Ca^{2+}, and BSA-Na$^+$-Ca^{2+} systems, respectively (Fig. 11). After NaOH cleaning, the fluxes of the BSA, BSA—Na$^+$, BSA—Ca^{2+} and BSA-Na$^+$-Ca^{2+} systems recovered to 110 %, 98 %, 86 % and 98 % of the initial fluxes, respectively. For the BSA system, the membrane flux recovered to about 110 % of the initial membrane flux after NaOH cleaning. This slight flux overshoot is attributed to NaOH's efficient removal of protein fouling and residual surface contaminants, thereby restoring or reopening transport pathways. Concurrently, a moderate reduction in water contact angle (from over 120° to 107°) enhances feed-to-membrane interface contact while maintaining

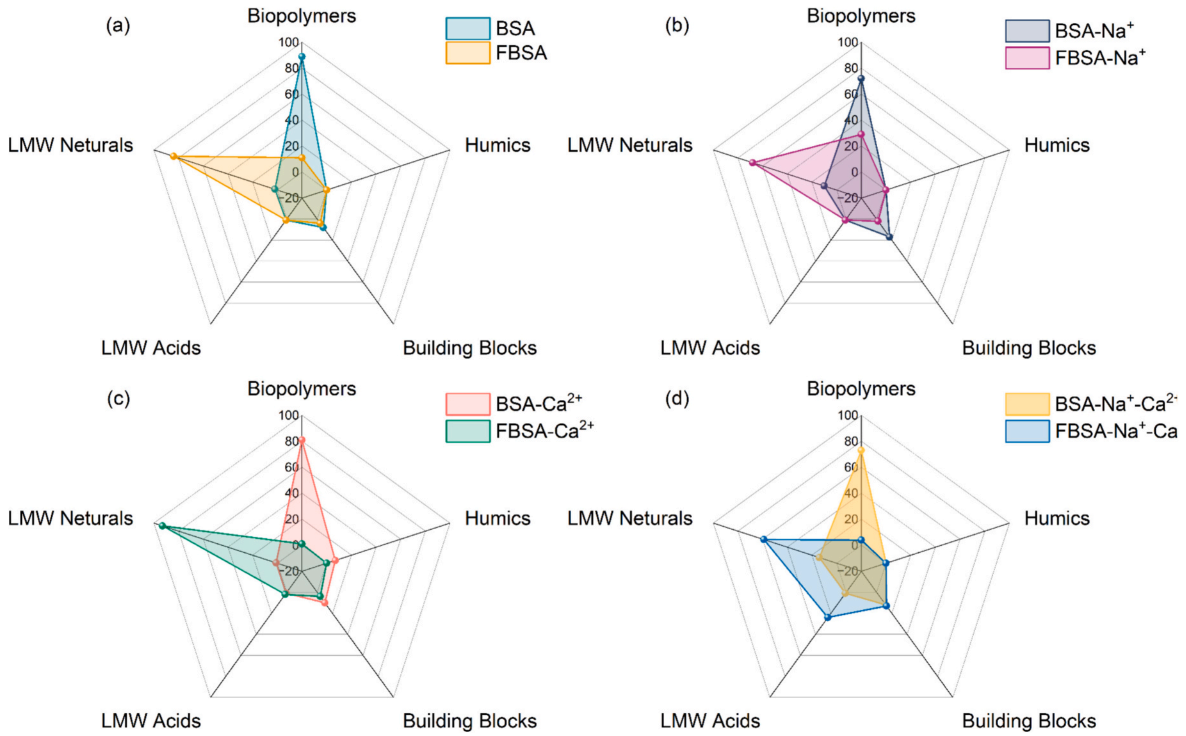

Fig. 10. Percentage change in CDOC components of feed liquid and fouling liquid.

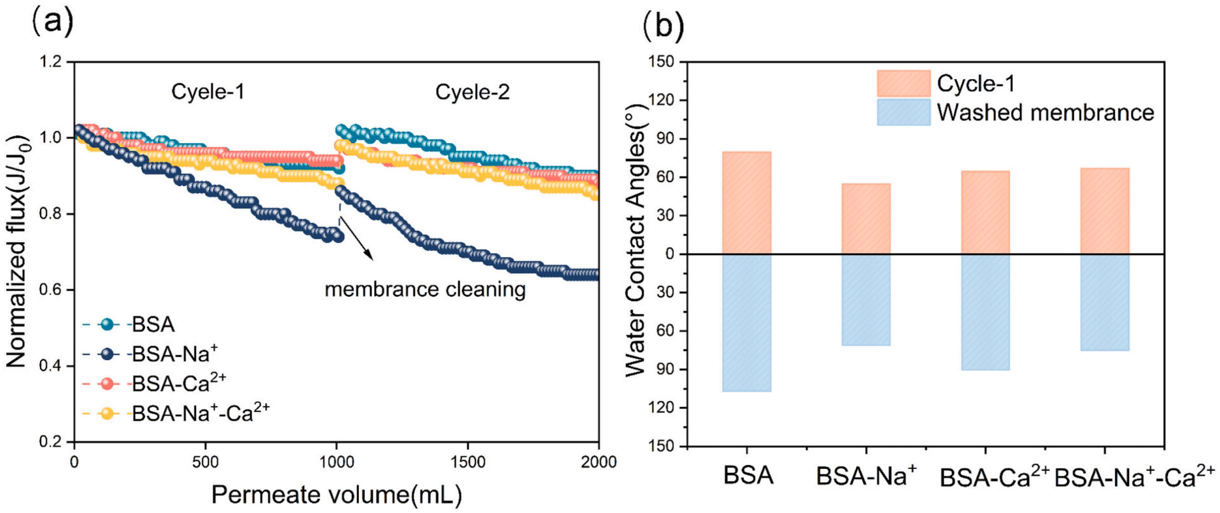

Fig. 11. (a) Normalized water flux in the membrane cleaning experiment, and (b) Water contact angles on the membrane surface.

sufficient membrane hydrophobicity. The water contact angles on the membrane surfaces of the BSA, BSA—Na$^+$, BSA—Ca^{2+} and BSA-Na$^+$-Ca^{2+} systems recovered to 106.9°, 71.0°, 90.1°, and 74.8°, respectively, indicating that the presence of inorganic salt ions reduced membrane cleaning efficiency. The BSA—Ca^{2+} system exhibited the lowest flux recovery ratio (86 %), suggesting that a portion of the foulants remained on the membrane surface. NaOH effectively removes loosely bound surface contaminants but it exhibits limited capacity to disrupt the stable BSA—Ca^{2+} complexes formed via ionic bridging. In the BSA—Na$^+$ system, the increased membrane hydrophilicity indicates that NaOH disrupted the hydrophobic adsorption structures induced by Na$^+$. Furthermore, the relatively high flux recovery ratio in the BSA—Na$^+$ system implies that residual BSA—Na$^+$ complexes are more readily removed.

To further elucidate the influence of cations on cleaning behavior, SEM imaging analysis was conducted on NaOH-cleaned membranes from the four fouling systems (Fig. 12). In the BSA system, the original fouling layer was largely removed, with the PTFE fiber network re-exposed and only scattered protein patches remaining on the surface. This observation is consistent with the high flux recovery and only a slight decrease in water contact angle. In the BSA—Na$^+$ system, the residual layer was thinner yet more continuous, partially retaining connections to the fiber network. In contrast, the BSA—Ca^{2+} system exhibited thicker, more adherent, and more heterogeneous residual deposits covering most pores and fiber intersections, indicating that NaOH could not effectively remove strongly bound BSA—Ca^{2+} complexes. The mixed BSA–Na$^+$–Ca^{2+} system exhibited mottled, plate-like residues partially covering the fiber network, resulting in a cleaning performance intermediate between the single-cation systems. Overall, the extent and morphology of the residual fouling layer strongly depend

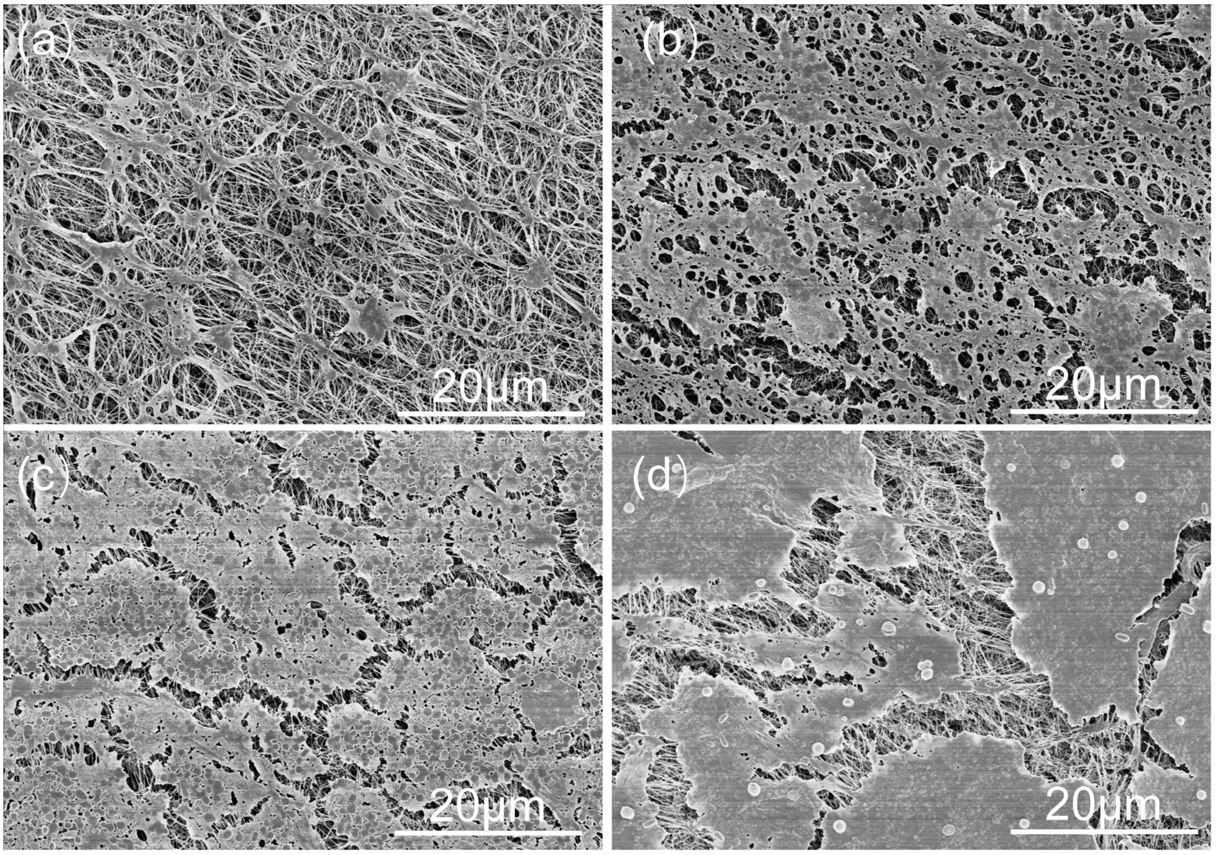

Fig. 12. The membrane surface after NaOH cleaning (a) BSA, (b) BSA—Na^+, (c) BSA—Ca^{2+}, and (d) BSA-Na^+-Ca^{2+} systems.

on the cationic composition present during the fouling process.

4. Conclusions

This study examined how monovalent Na^+ and divalent Ca^{2+} influence BSA fouling in MD and clarified the underlying mechanisms. The results show that both cations induce membrane fouling, yet the majority of the foulant layer can be removed through post-cleaning. Upon cation addition, EL interactions are markedly attenuated, allowing AB forces to dominate and thereby increasing the adsorption of LMW Neutrals species on the membrane surface. Ca^{2+} concentration and particle size both exhibit positive correlations with zeta potential, indicating that Ca^{2+} primarily influences fouling by modifying colloidal size and surface charge. Na^+ concentration displays a strong negative correlation with membrane flux, and Na-induced fouling is more severe because Na^+ lowers the interaction energy barrier to its minimum and promotes the accumulation of hydrophobic foulants. In the mixed BSA-Na^+-Ca^{2+} system, competitive interactions between the two cations yield an intermediate degree of fouling relative to the single-cation systems.

CRediT authorship contribution statement

Mingmei Ding: Writing – original draft, Validation, Methodology, Data curation. **Beining Liu:** Data curation, Visualization. **Sihao Zhang:** Investigation, Methodology. **Ao Wang:** Investigation, Formal analysis. **Hang Xu:** Writing – review & editing, Funding acquisition. **Emily Gao:** Methodology. **Jianhua Zhang:** Resources. **Long D. Nghiem:** Validation. **Li Gao:** Supervision, Conceptualization, Project administration.

Declaration of competing interest

The authors declare that they have no known competing financial interests or personal relationships that could have appeared to influence the work reported in this paper.

Acknowledgments

This work was financially supported by National Natural Science Foundation of China (No. 52200011), Natural Science Foundation of Jiangsu Province (No. BK20220989), National Key Research and Development Program of China (2022YFC3203702).

Appendix A. Supplementary data

Supplementary data to this article can be found online at https://doi.org/10.1016/j.desal.2025.119734.

Data availability

Data will be made available on request.

References

[1] F.C.R. Costa, B.C. Ricci, B. Teodoro, K. Koch, J.E. Drewes, M.C.S. Amaral, Biofouling in membrane distillation applications - a review, Desalination 516 (2021) 115241.

[2] E. Gontarek-Castro, R. Castro-Muñoz, How to make membrane distillation greener: a review of environmentally friendly and sustainable aspects, Green Chem. 26 (1) (2024) 164–185.

[3] S. Zhao, C. Jiang, J. Fan, S. Hong, P. Mei, R. Yao, Y. Liu, S. Zhang, H. Li, H. Zhang, C. Sun, Z. Guo, P. Shao, Y. Zhu, J. Zhang, L. Guo, Y. Ma, J. Zhang, X. Feng, F. Wang, H. Wu, B. Wang, Hydrophilicity gradient in covalent organic frameworks for membrane distillation, Nat. Mater. 20 (11) (2021) 1551–1558.

[4] F.E. Ahmed, B.S. Lalia, R. Hashaikeh, N. Hilal, Alternative heating techniques in membrane distillation: a review, Desalination 496 (2020) 114713.

[5] M. Xu, J. Cheng, X. Du, Q. Guo, Y. Huang, Q. Huang, Amphiphobic electrospun PTFE nanofibrous membranes for robust membrane distillation process, J. Membr. Sci. 641 (2022) 119876.

[6] A. Abdel-Karim, S. Leaper, C. Skuse, G. Zaragoza, M. Gryta, P. Gorgojo, Membrane cleaning and pretreatments in membrane distillation – a review, Chem. Eng. J. 422 (2021) 129696.

[7] M. Qasim, I.U. Samad, N.A. Darwish, N. Hilal, Comprehensive review of membrane design and synthesis for membrane distillation, Desalination 518 (2021) 115168.

[8] A. Yadav, P.K. Labhasetwar, V.K. Shahi, Membrane distillation using low-grade energy for desalination: a review, J. Environ. Chem. Eng. 9 (5) (2021) 105818.

[9] A. Narayan, R. Pitchumani, Analysis of an air-cooled air gap membrane distillation module, Desalination 475 (2020) 114179.

[10] R. Ullah, M. Khraisheh, R.J. Esteves, J.T. McLeskey, M. AlGhouti, M. Gad-el-Hak, H. Vahedi Tafreshi, Energy efficiency of direct contact membrane distillation, Desalination 433 (2018) 56–67.

[11] B.B. Ashoor, S. Mansour, A. Giwa, V. Dufour, S.W. Hasan, Principles and applications of direct contact membrane distillation (DCMD): a comprehensive review, Desalination 398 (2016) 222–246.

[12] V. Okati, A.J. Moghadam, M. Farzaneh-Gord, M. Moein-Jahromi, Thermo-economical and environmental analyses of a direct contact membrane distillation (DCMD) performance, J. Clean. Prod. 340 (2022) 130613.

[13] F. Ricceri, B. Blankert, N. Ghaffour, J.S. Vrouwenvelder, A. Tiraferri, L. Fortunato, Unraveling the role of feed temperature and cross-flow velocity on organic fouling in membrane distillation using response surface methodology, Desalination 540 (2022) 115971.

[14] Y. Ma, J.W. Chew, Investigation of membrane fouling phenomenon using molecular dynamics simulations: a review, J. Membr. Sci. 661 (2022) 120874.

[15] J. Kim, H.-W. Kim, L.D. Tijing, H.K. Shon, S. Hong, Elucidation of physicochemical scaling mechanisms in membrane distillation (MD): implication to the control of inorganic fouling, Desalination 527 (2022) 115573.

[16] F. Ricceri, B. Blankert, L. Ranieri, C. Picioreanu, N. Ghaffour, J.S. Vrouwenvelder, A. Tiraferri, L. Fortunato, Understanding the evolution of organic fouling in membrane distillation through driving force and resistance analysis, J. Membr. Sci. 686 (2023) 121993.

[17] W.J. Lee, Z.C. Ng, S.K. Hubadillah, P.S. Goh, W.J. Lau, M.H.D. Othman, A.F. Ismail, N. Hilal, Fouling mitigation in forward osmosis and membrane distillation for desalination, Desalination 480 (2020) 114338.

[18] L. Liu, Z. Xiao, Y. Liu, X. Li, H. Yin, A. Volkov, T. He, Understanding the fouling/scaling resistance of superhydrophobic/omniphobic membranes in membrane distillation, Desalination 499 (2021) 114864.

[19] C. Liu, L. Chen, L. Zhu, Fouling mechanism of hydrophobic polytetrafluoroethylene (PTFE) membrane by differently charged organics during direct contact membrane distillation (DCMD) process: an especial interest in the feed properties, J. Membr. Sci. 548 (2018) 125–135.

[20] F. Tibi, A. Charfi, J. Cho, J. Kim, Effect of interactions between ammonium and organic fouling simulated by sodium alginate on performance of direct contact membrane distillation, Sep. Purif. Technol. 278 (2021) 119551.

[21] Y.Z. Tan, J.W. Chew, W.B. Krantz, Effect of humic-acid fouling on membrane distillation, J. Membr. Sci. 504 (2016) 263–273.

[22] E. Celik, L. Liu, H. Choi, Protein fouling behavior of carbon nanotube/polyethersulfone composite membranes during water filtration, Water Res. 45 (16) (2011) 5287–5294.

[23] D. Hou, D. Lin, C. Zhao, J. Wang, C. Fu, Control of protein (BSA) fouling by ultrasonic irradiation during membrane distillation process, Sep. Purif. Technol. 175 (2017) 287–297.

[24] K. Valta, P. Damala, E. Angeli, G. Antonopoulou, D. Malamis, K.J. Haralambous, Current treatment Technologies of Cheese Whey and Wastewater by Greek cheese manufacturing units and potential valorisation opportunities, Waste Biomass Valoriz. 8 (5) (2017) 1649–1663.

[25] Y. Zhai, D. Bai, Y. Wang, Y. Zhang, Y. Qi, X. Qiu, Y.-f. Wang, Y.x. Wang, X. Zheng, Effect of Na+ on organic fouling depends on Na+ concentration and the property of the foulants, Desalination 531 (2022) 115709.

[26] Y. Ding, B. Ma, H. Liu, J. Qu, Effects of protein properties on ultrafiltration membrane fouling performance in water treatment, J. Environ. Sci. 77 (2019) 273–281.

[27] W. Cai, J. Zhang, Y. Li, Q. Chen, W. Xie, J. Wang, Characterizing membrane fouling formation during ultrafiltration of high-salinity organic wastewater, Chemosphere 287 (2022) 132057.

[28] B. Zhang, H. Tang, J. Chen, B. Zhang, Y. Shen, W. Shi, New mechanistic insights into the effect of cations on membrane fouling caused by anionic polyacrylamide, J. Colloid Interface Sci. 606 (2022) 10–21.

[29] H. Mo, K.G. Tay, H.Y. Ng, Fouling of reverse osmosis membrane by protein (BSA): effects of pH, calcium, magnesium, ionic strength and temperature, J. Membr. Sci. 315 (1) (2008) 28–35.

[30] A. Tiraferri, Y. Kang, E.P. Giannelis, M. Elimelech, Superhydrophilic thin-film composite forward osmosis membranes for organic fouling control: fouling behavior and antifouling mechanisms, Environ. Sci. Technol. 46 (20) (2012) 11135–11144.

[31] Y.-N. Wang, C.Y. Tang, Fouling of Nanofiltration, reverse osmosis, and ultrafiltration membranes by protein mixtures: the role of inter-foulant-species interaction, Environ. Sci. Technol. 45 (15) (2011) 6373–6379.

[32] Y. Meng, Q. Zhong, Y. Liu, Z. Yan, Y. Liang, H. Chang, H. Liang, R.D. Vidic, Evaluating membrane cleaning for organic fouling in direct contact membrane distillation, J. Clean. Prod. 410 (2023) 137319.

[33] Q.-M. Nguyen, S. Jeong, S. Lee, Characteristics of membrane foulants at different degrees of SWRO brine concentration by membrane distillation, Desalination 409 (2017) 7–20.

[34] T. Zhang, J. Zhang, Q. Wang, H. Zhang, Z. Wang, Z. Wu, Evaluating of the performance of natural mineral vermiculite modified PVDF membrane for oil/water separation by membrane fouling model and XDLVO theory, J. Membr. Sci. 641 (2022) 119886.

[35] D. Hou, Z. Yuan, M. Tang, K. Wang, J. Wang, Effect and mechanism of an anionic surfactant on membrane performance during direct contact membrane distillation, J. Membr. Sci. 595 (2020) 117495.

[36] H. Wu, F. Shen, J. Wang, Y. Wan, Membrane fouling in vacuum membrane distillation for ionic liquid recycling: interaction energy analysis with the XDLVO approach, J. Membr. Sci. 550 (2018) 436–447.

[37] W.H. Abuwatfa, N. AlSawaftah, N. Darwish, W.G. Pitt, G.A. Husseini, A review on membrane fouling prediction using artificial neural networks (ANNs), Membranes 13 (7) (2023) 685.

[38] D.C. Sobeck, M.J. Higgins, Examination of three theories for mechanisms of cation-induced bioflocculation, Water Res. 36 (3) (2002) 527–538.

[39] B. Li, X. He, P. Wang, Q. Liu, W. Qiu, J. Ma, Opposite impacts of K+ and Ca2+ on membrane fouling by humic acid and cleaning process: evaluation and mechanism investigation, Water Res. 183 (2020) 116006.

[40] A. Boubakri, A. Hafiane, S.A.T. Bouguecha, Direct contact membrane distillation: capability to desalt raw water, Arab. J. Chem. 10 (2017) S3475–S3481.

[41] D. Qu, J. Wang, L. Wang, D. Hou, Z. Luan, B. Wang, Integration of accelerated precipitation softening with membrane distillation for high-recovery desalination of primary reverse osmosis concentrate, Sep. Purif. Technol. 67 (1) (2009) 21–25.

[42] F. Qiu, Y. Sun, Y. Zhang, H. Liu, L. Shao, Q. Huang, Electrospun PTFE nanofibrous composite membranes featuring a fiber network structure for organic solvent nanofiltration (OSN), Sep. Purif. Technol. 330 (2024) 125416.

[43] W. Chen, C. Qian, K.-G. Zhou, H.-Q. Yu, Molecular spectroscopic characterization of membrane fouling: a critical review, Chem 4 (7) (2018) 1492–1509.

[44] J. Grdadolnik, Y. Maréchal, Bovine serum albumin observed by infrared spectrometry. I. Methodology, structural investigation, and water uptake, Biopolymers 62 (1) (2001) 40–53.

[45] H.A. Alhazmi, FT-IR spectroscopy for the identification of binding sites and measurements of the binding interactions of important metal ions with bovine serum albumin, Sci. Pharm. 87 (1) (2019) 5.

[46] C. Guo, X. Guo, W. Chu, N. Jiang, H. Li, Spectroscopic study of conformation changes of bovine serum albumin in aqueous environment, Chin. Chem. Lett. 30 (6) (2019) 1302–1306.

[47] S. Liang, Y. Zhao, C. Liu, L. Song, Effect of solution chemistry on the fouling potential of dissolved organic matter in membrane bioreactor systems, J. Membr. Sci. 310 (1) (2008) 503–511.

[48] T. Lin, B. Shen, W. Chen, X. Zhang, Interaction mechanisms associated with organic colloid fouling of ultrafiltration membrane in a drinking water treatment system, Desalination 332 (1) (2014) 100–108.

[49] T. Lin, Z. Lu, W. Chen, Interaction mechanisms of humic acid combined with calcium ions on membrane fouling at different conditions in an ultrafiltration system, Desalination 357 (2015) 26–35.

[50] X. Yu, T. Lin, H. Xu, H. Tao, W. Chen, Ultrafiltration of up-flow biological activated carbon effluent: extracellular polymer biofouling mechanism and mitigation using pre-ozonation with H2O2 backwashing, Water Res. 186 (2020) 116391.

[51] W. Liu, B. Liu, X. Li, UV/Fe(II) synergistically activated S(IV) per-treatment on HA-enhanced Ca2+ scaling in NF filtration: fouling mitigation, mechanisms and correlation analysis of membrane resistance in different filtration stage, Chemosphere 308 (2022) 136302.

[52] N. Subhi, G. Leslie, V. Chen, P. Le-Clech, Organic fouling of ultrafiltration membrane: detailed characterization by liquid chromatography with organic carbon detector (LC-OCD), Sep. Sci. Technol. 48 (2) (2012) 199–207.

[53] S. Park, T. Nam, J. You, E.-S. Kim, I. Choi, J. Park, K.H. Cho, Evaluating membrane fouling potentials of dissolved organic matter in brackish water, Water Res. 149 (2019) 65–73.

[54] S.A. Huber, A. Balz, M. Abert, W. Pronk, Characterisation of aquatic humic and non-humic matter with size-exclusion chromatography – organic carbon detection – organic nitrogen detection (LC-OCD-OND), Water Res. 45 (2) (2011) 879–885.